



# Seismic structure beneath the Tonga arc and Lau back-arc basin determined from joint Vp, Vp/Vs tomography

**James A. Conder and Douglas A. Wiens**

*Department of Earth and Planetary Sciences, Washington University, Campus Box 1169, One Brookings Drive, St. Louis, Missouri 63130, USA (conder@seismo.wustl.edu)*

[1] The Tonga arc and associated Lau basin exhibit many geologically important processes that link subduction and mantle flow with plate separation and crustal production. We create seismic tomograms of the Tonga-Lau region by jointly inverting for Vp and Vp/Vs structure using data from the LABATTS ocean bottom seismograph experiment and several island deployments to better constrain dynamic processes in the mantle wedge. Jointly using *P* and *S* data can help distinguish between the various mechanisms responsible for seismic velocity anomalies such as temperature and the presence of melt and/or volatiles. Because high attenuation in the wedge limits the *S* wave data set, we focus on 2-D inversions beneath the linear OBS array where resolution is best and also parameterize the solution in terms of the Vp/Vs ratio. As expected, the subducting slab has fast Vp and Vs and a low Vp/Vs ratio, consistent with the cold downgoing plate. The Central Lau Spreading Center (CLSC) exhibits stronger anomalies in Vp/Vs than in Vp, with the anomalies larger than would be predicted purely by temperature variations. The CLSC anomaly extends >100 km to the west of the axis, suggesting a broad region of melt production driven by passive upwelling from plate separation rather than active upwelling mechanisms. The anomaly is asymmetric about the axis, suggesting that slab-induced corner flow possibly influences mantle dynamics several hundred kilometers away from the arc. There is a strong anomaly beneath the volcanic arc that gradually deepens as it trends toward the back arc, likely outlining a hydrated region of melt production that feeds the volcanic front. Hydration possibly continues throughout the wedge to at least 400 km depth. The Lau ridge exhibits a thicker lithosphere relative to the rest of the Basin, while the Fiji platform likely has a thinner lithosphere than the Lau Ridge from more recent extension. There is also a reasonable likelihood of a small degree of partial melt in the uppermost mantle beneath the platform.

**Components:** 13,796 words, 10 figures.

**Keywords:** back-arc basin; Fiji; island arc; Lau; subduction; tomography.

**Index Terms:** 3001 Marine Geology and Geophysics: Back-arc basin processes; 7270 Seismology: Tomography (6982, 8180); 8170 Tectonophysics: Subduction zone processes (1031, 3060, 3613, 8413).

**Received** 12 August 2005; **Revised** 15 December 2005; **Accepted** 27 January 2006; **Published** 31 March 2006.

Conder, J. A., and D. A. Wiens (2006), Seismic structure beneath the Tonga arc and Lau back-arc basin determined from joint Vp, Vp/Vs tomography, *Geochem. Geophys. Geosyst.*, 7, Q03018, doi:10.1029/2005GC001113.

## 1. Introduction

[2] Back-arc basins and associated volcanic arcs are key geological systems in the development and recycling of the Earth's crust with many geologically significant and intertwining processes associated with subduction, melting, and basin dynamics. For example, magmatism at volcanic arcs is de-

rived from varying degrees of wedge hydration from the slab [Cameron *et al.*, 2003; Roggensack *et al.*, 1997; Walker *et al.*, 1995], decompression melting in the corner [Conder *et al.*, 2002a; Sisson and Bronto, 1998; Walker *et al.*, 1995], and possibly slab sediment melting [Conder, 2005; Johnson and Plank, 1999]; Each of these mechanisms may produce spatially different melt regions. The Lau

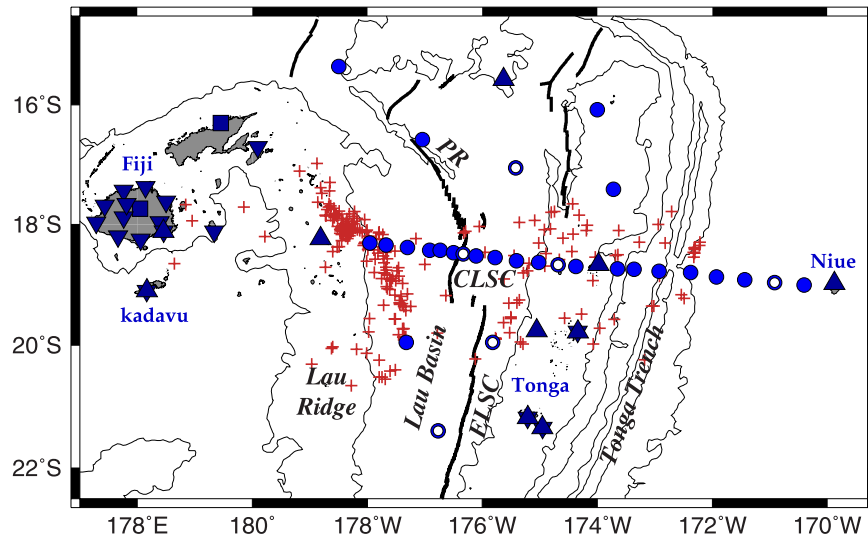


**Figure 1.** Map of the study area. Thick, black lines show spreading center geometry. Thin lines are 1 km bathymetric contours from ETOPO5 [Smith and Sandwell, 1997]. Circles show ocean bottom seismograph locations. One additional OBS is located outside the boundaries of the figure at 22.1°S, 179.6°W. Circles containing white dots are OBS locations with no data recovery due to equipment failure. Triangles mark island seismograph stations. Triangles pointing up are from the SPASE experiment [Wiens *et al.*, 1995], and downward pointing triangles are from the SAFT experiment [Tibi and Wiens, 2005]. A few stations were used in both deployments, such as the station on the southern island of Kandavu. Two IRIS stations that were also used are denoted as squares. Tomographic cross section is along the main line of ocean bottom seismographs, extending from Fiji in the west to Niue in the East. Only stations along the main line along with three island stations just south of the line were used in the tomography, while the others were only used for hypocenter location. Red crosses denote 226 earthquake locations used in this study.

Basin between Fiji and Tonga has long been considered a type example of active back-arc tectonics [Karig, 1971]. This consideration has recently been underscored by the selection of the Eastern Lau Spreading Center (ELSC) as a focus site of the U.S. RIDGE 2000 program ([http://www.ridge2000.org/science/info/science\\_plan.html](http://www.ridge2000.org/science/info/science_plan.html)).

[3] The Lau Basin has likely undergone several episodes of rifting and subsequent seafloor spreading in the back arc during its geological history [Martinez and Taylor, 2002; Parson and Hawkins, 1994; Taylor *et al.*, 1996]. The current stage of rifting in the Lau basin began at 4–6 Ma, beginning in the northern section of the basin and propagating southward [Taylor *et al.*, 1996]. The Lau spreading system comprises a number of robust spreading centers roughly north-south orientated trends extending from 15°S to 24°S (Figure 1), with slower diffuse rifting further south in the Havre Trough [Fujiwara *et al.*, 2001]. Rates along the southernmost Eastern Lau spreading center increase from <3 cm/yr at the southern terminus to ~9 cm/yr near 19°30'S [Zellmer and Taylor, 2001]. Northward, the spreading system moves from the ELSC to the Central Lau Spreading Center (CLSC) via a ~50 km overlapping

spreading center discontinuity. The CLSC is a ~110 km long fast spreading segment with a spreading rate of 8.5 cm/yr [Zellmer and Taylor, 2001]. To the north, the CLSC terminates at an extensional relay zone and Peggy Ridge (PR) transform fault [Eguchi *et al.*, 1989]. The northern Lau basin, where full spreading rates are greatest (~15 cm/yr [Bevis *et al.*, 2000]), comprises several microplates with sub-parallel spreading boundaries that each account for a portion of the full rate of extension [Pelletier *et al.*, 2001; Zellmer and Taylor, 2001].

[4] Because the Tonga slab beneath the Lau back arc is the most seismically active Wadati-Benioff zone in the world, the Tonga-Lau region is one of the best locations for detailed imaging of the slab and mantle wedge structure. There is a rich history of seismological studies on these topics dating back to the advent of plate tectonics, and many phenomena, such as back-arc basins with low seismic velocity and high attenuation, were first identified in this location [Aggarwal *et al.*, 1972; Barazangi *et al.*, 1973; Hamburger and Isacks, 1987; Isacks *et al.*, 1969; Sykes *et al.*, 1969]. Several more recent studies have determined tomographic models of this region [Gorbatov and Kennett, 2003; Kolobov *et al.*, 2003; van der Hilst,

1995], delineating the Tonga Benioff Zone as a high-velocity slab with a low-velocity region in the Lau back arc. However, these studies using teleseismic arrival times lack the spatial resolution necessary for detailed studies and modeling of arc and back-arc processes.

[5] Several of the recent seismic studies of this region result from a data set collected by the SPASE deployment of 12 land seismic stations from 1993–1995 [Wiens *et al.*, 1995] and the contemporaneous 3 month LABATTS deployment of ocean bottom seismographs (OBS). Most of the 30 OBSs in this experiment were deployed in a linear array across the CLSC and Tonga arc (Figure 1) to image the mantle wedge structure beneath the central Lau basin. Zhao *et al.* [1997] used the  $P$  wave data set from this experiment to determine a new, more detailed 3-D  $P$  wave tomographic model that showed low  $P$  velocity within the upper 400 km of the mantle wedge. The lowest mantle  $P$  velocities were immediately westward of the CLSC and beneath the Tonga volcanic arc. Attenuation tomography also showed extremely high attenuation beneath the Lau back arc [Roth *et al.*, 1999], and waveform inversion showed extremely slow shear velocities at depths of 30–90 km beneath the Lau basin [Xu and Wiens, 1997]. Koper *et al.* [1999] used  $P$  and  $S$  wave travel times from selected earthquakes to investigate the fractional change in  $S$  velocity relative to  $P$  velocity ( $d\ln V_s/d\ln V_p$ , often denoted as  $\nu$ ). They found that  $\nu$  was about 1.2–1.3 throughout the entire region, inconsistent with the occurrence of widespread melt in the upper mantle of the Lau Basin for experimentally determined models of melt geometry [e.g., Hammond and Humphreys, 2000], suggesting that temperature controls the broad variations in seismic velocity structure throughout the wedge.

[6] There are two major limitations with the previous work. First, the Zhao *et al.* [1997] study does not include any  $S$  wave data, and therefore there are no  $V_p/V_s$  constraints on the material properties and the possible distribution of melt. Second, the Koper *et al.* [1999] study only solved for  $\nu$  of the bulk mantle wedge, and provides no information on how the  $V_p/V_s$  ratio may vary within the wedge. In this paper, we expand on these and other prior studies by using both  $P$  wave and  $S$  wave data from the OBS and island stations in the Lau Basin, as well as island station data from a new study carried out in 2001–2002 [Tibi and Wiens, 2005], to jointly invert for  $V_p$  and  $V_p/V_s$  structure throughout the wedge. Correlating the spatial distribution

and magnitudes of  $V_p$  and  $V_p/V_s$  anomalies derived by a joint  $V_p$  and  $V_p/V_s$  tomography will help shed light on the overall wedge and slab structure, advance our understanding of such geologic processes as wedge hydration and melt generation/interaction and delineate regions within the wedge containing partial melt and/or volatiles.

## 2. Data

[7] Strong attenuation of  $S$  waves caused by the low  $Q$  back arc [Roth *et al.*, 1999] restricts the observations of  $S$  waves in the back arc to the larger earthquakes, and provides only a limited  $S$  wave data set. This  $S$  wave data set is inadequate for good 3-D  $S$  wave tomography, and in addition, both  $P$  and  $S$  3-D velocity models would be best resolved along the E-W line of OBSs compared to elsewhere in the model. Therefore, in this study we focus on using available high quality travel times to create 2-D  $V_p$  and  $V_p/V_s$  structures. Our 2-D tomography grid extends 700 km deep and 1400 km across from west of the Fiji platform, along the OBS line and ending at Niue Island on the Pacific plate. Hypocenters used in this study are within  $\sim 125$  km of the cross-section line (Figure 1). We include a few deep events a little further to the south, as the slab is relatively 2-D in that direction. For our tomographic analysis, we use 2261  $P$  wave arrivals and 886  $S$  wave arrivals from 226 local earthquakes. All of the  $S$  observations were recorded by the local stations and the paths are fully contained within the box defined for this tomographic study (Figure 2). 438 of the  $P$  paths are from sources inside the box and arrive at teleseismic stations reasonably aligned with our cross section, such as Port Moresby, Papua New Guinea to the west and Rarotonga in the Cook Islands to the east. These teleseismic rays are typically downgoing so they provide information about portions of the model space that are otherwise largely devoid of local ray paths. In addition to the previously determined  $P$  wave arrival times from the LABATTS OBS experiment [Koper *et al.*, 1999; Zhao *et al.*, 1997] and the island-based SPASE [Wiens *et al.*, 1995] deployments, we determined additional  $S$  wave arrival times and added additional  $P$  and  $S$  observations from the 2001–2002 SAFT [Tibi and Wiens, 2005] experiment.

[8] The land seismic stations were equipped with STS-2 and Guralp-3T and 40T broadband sensors; the OBSs used 1 Hz L-4 sensors. Where possible, arrivals are picked from the unfiltered waveforms. Otherwise,  $P$  data are typically filtered with a 0.6

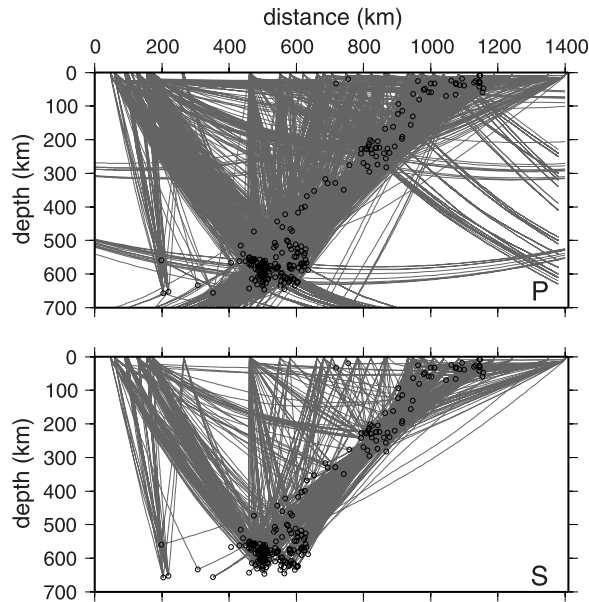


**Figure 2.** Ray coverage projected onto 2-D plane used for cross section. The top panel shows *P* wave ray coverage, and the bottom panel shows *S* wave ray coverage. Black circles show hypocenters which delineate the slab to >650 km depth. 1823 *P* paths are fully contained within the model space, and 438 are the source-side portion of teleseismic arrivals (see text for their treatment in the inversion). All 886 *S* paths are fully contained within the model space.

or 1 Hz highpass filter and *S* data in the back arc were typically filtered with a 0.02 – 0.2 Hz bandpass, as the observed noise peaks around 0.3 Hz and local *P* arrivals are characteristically higher frequency than *S* arrivals. We also include 10,283 teleseismic arrival times, primarily from the USGS preliminary determination of epicenters (PDE) catalog and to a lesser extent from the International Seismological Centre (ISC), for determination of hypocenter locations. Handpicked data were each assigned a standard deviation (usually 0.1–0.3s for *P* and 0.2–0.5 for *S*) on the basis of the quality of the pick and weighted accordingly in the inversion. PDE and ISC arrival times were assigned standard deviations of 0.3s for *P* waves and 0.5s for *S* waves.

[9] Both *P* and *S* were picked on the first arrival; thus *S* wave times denote the fast arrival when the seismograph components show slightly differing arrival times due to shear wave splitting. Because of seismic anisotropy in the region [Smith *et al.*, 2001], this can introduce some bias into the data set. Smith *et al.* [2001] show splitting times for *S* arrivals of up to 1 second on the Fiji plateau and near the forearc. With this in mind, *V<sub>p</sub>/V<sub>s</sub>* ratios in this study should be considered minimum esti-

mates. Most of the highly split *S* wave ray paths have a length of 450 km or greater; for this length and a splitting time of 1 second, the *V<sub>p</sub>/V<sub>s</sub>* value would be underestimated by about 0.02. This magnitude of underestimation is likely not a significant issue over most of the model space, as resolved *V<sub>p</sub>/V<sub>s</sub>* variations are on the order of 0.1, but this concern should be kept in mind for interpretation of individual features.

[10] To include outgoing rays in our inversion, we break the ray path into two parts: that portion inside the tomography box, and the portion outside the box. We determine the complete ray path with a gridsearch over the edge of the box that minimizes the sum of the travel times of the two segments. We calculate travel times within the box from the 2-D velocity model, while those outside the box are calculated assuming the AK135 velocity model [Kennett *et al.*, 1995] with corrections for station elevations. We account for a receiver-side travel time anomaly by including a station correction model parameter in the inversion for each teleseismic station. Only stations with at least 8 arrivals are used. We attempted to use arrivals at stations within the study region from teleseismic sources, but because of the short duration of the LABATTS deployment, there are too few events located approximately along the strike of our 2-D plane to contribute significantly to the solution.

[11] As with any least squares inverse problem, the existence of outliers influences the results, so it is useful to suppress unreliable data. But, within a heterogeneous medium, many reliable data may have fairly large residuals relative to a starting model (for instance slab paths in a 1-D velocity model), so we are reluctant to eliminate databased on a residual cutoff. We address outliers in a fashion similar to the uniform reduction method of Jeffreys [1932] adopted by the International Seismological Centre [e.g., Willemann, 2001]. To keep all the useful data, but reduce the impact of outliers, we adjust all data weights by a factor, *w*, determined by

$$w = 1 / (1 + \mu \exp(r^2 / 2\sigma^2)), \quad (1)$$

where *r* is the residual of the datum to the starting model (or previous iteration),  $\mu$  is assigned a value of 0.05, and  $\sigma$  is decided by the type of datum: 1 for *P* data within the box,  $\sqrt{2}$  for *S* data, and  $1/\sqrt{2}$  for teleseismic *P* (Figure 3). With this method, the model will be fit to consistent, but large, residuals while minimizing the bias introduced from outliers. With further iterations, the fit to data containing real

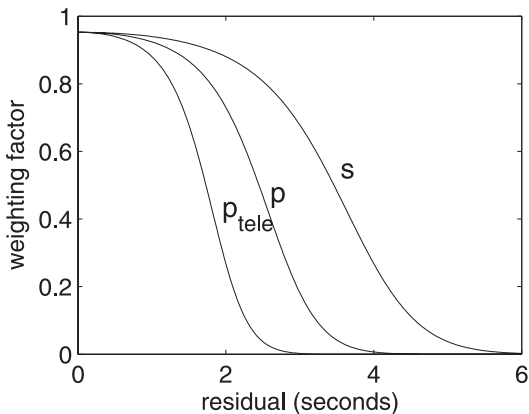


**Figure 3.** Dynamic weighting scheme for the data following the Uniform Reduction Method of *Jeffreys* [1932]. Less weight is given to data with large residuals, thereby limiting biases from outliers. With further iterations, consistent data will be upweighted while inconsistent data are considered outliers and carry minimal weight.

signal will improve (increasing their weight), while true outliers will continue to carry minimal weight.

### 3. Methods

[12] We reference all anomalies in the tomographic models to a best fitting 1-D model for our data

(Figure 4). We invert for the 1-D model using a least squares inversion similar to that used in our tomography, but with considerably fewer model parameters. To stabilize the profile, the 1-D inversion result is penalized against the 1-D North Fiji Basin (NFB) velocity model of *Wiens et al.* [2006], and includes a first derivative smoothing function. SV and SH velocities of *Wiens et al.* [2006] are determined by inversions of Love and Rayleigh waves across the array, while P is determined by assuming a  $d \ln V_s / d \ln V_p$  of 1.3 referenced against IASP91 [*Kennett and Engdahl*, 1991]. Below 200 km depth we increasingly penalize the function against IASP91 as the NFB model (determined by surface waves) has decreasing resolution and there is less reason to expect significant deviations from global velocity models at depth. Thus our best fitting velocity structure is slightly faster than IASP91 below 200 km depth ( $\sim 0.05$  km/s), but considerably slower at shallower depths (Figure 4).  $V_p/V_s$  below 200 km is close to IASP91 structure but varies by as much as 0.03 at shallower levels. The overall slowness at shallower depths is not unexpected, as the Lau Basin may exhibit the warmest mantle wedge of any back-arc basin (other than the North Fiji Basin just to the north of the Lau with multiple spreading centers and even slower shear wave velocities) [*Wiens et al.*, 2004; *Xu and Wiens*, 1997]. The slightly fast anomaly relative to

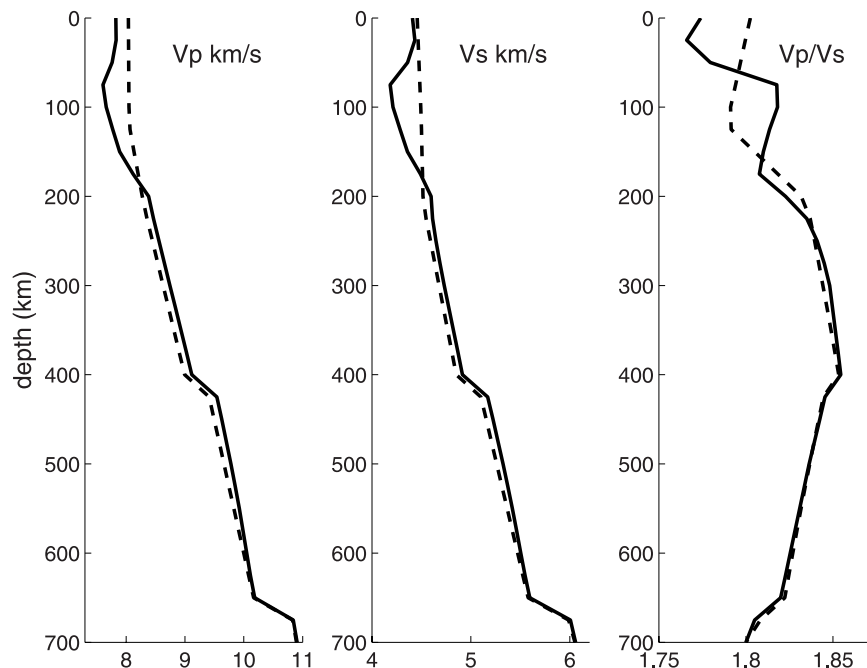


**Figure 4.** Best fitting 1-D velocity and  $V_p/V_s$  models for given data set (solid). Anomalies in tomography are referenced to these profiles. Both  $V_p$  and  $V_s$  show a low-velocity zone near 75 km depth. Below 200 km, profiles are similar to the IASP91 global model (dashed) [*Kennett and Engdahl*, 1991].

IASP91 below 200 km depth is also expected, as the slab velocity contributes to the overall average.

[13] A few different approaches have been used in the literature for calculating Vp/Vs tomographic models. With excellent ray coverage in both P and S waves, such as in Japan, Vp/Vs has been determined by inverting separate Vp and Vs models tied together only by hypocenter locations [Nakajima *et al.*, 2001; Nakamura *et al.*, 2003]. When S wave coverage is not as robust as P wave coverage, as is often the case, S-P times have been used to determine Vp/Vs [Chiarabba and Amato, 2003; Walck, 1988]. The S-P method makes the assumption that the Vp model is perfectly constrained by the P arrivals and that the S paths are identical to the P paths. We prefer that the S model not be constrained by poorly resolved portions of the P-model, so we use a method that inverts simultaneously for Vp and Vp/Vs ratio and does not assume identical P and S paths.

[14] We use the Singular Value Decomposition (SVD) to jointly invert for the Vp velocity and Vp/Vs structures. Model parameters are P slownesses and Vp/Vs values at nodes spaced 25 km horizontally and vertically covering a 1400 km long by 700 km deep box. The slowness or Vp/Vs value at any particular location is assumed to be a linear combination of the 4 surrounding nodes [Zhao *et al.*, 1992]. In our model, we account for the curvature of the Earth by reshaping the grid of rectangular elements to a grid of trapezoidal elements and trace ray paths through the trapezoidal mesh. We trace the ray paths with a two-point bending technique [Um and Thurber, 1987], allowing for a refraction at the moho [Zhao *et al.*, 1992].

[15] Crustal structure clearly affects travel times and must be addressed either as (an) additional parameter(s) or as a correction. We do not invert for the velocity of the crust, so we remove that portion of the ray path from the inversion and make a correction to the observed travel time assuming a 6.0 km/s crust for P waves and 3.5 km/s for S waves. The assumed thickness of the crust is a constant for each station determined by seismic reflection [Crawford *et al.*, 2003] along the OBS line, and assumed to be 24 km thick plus station elevation on the Fiji platform [Hamburger *et al.*, 1990] and Tonga arc. Errors in assumed crustal structure will result in  $\sim 0.04$  s/km difference in travel time correction for both P and S arrivals, but by using the active source survey as our guide, we believe errors in the assumed crustal structure are minimal.

[16] We use the well-known forward equation for P wave travel time, which reduces to

$$t_p^* = t_p^{\text{pre}} + \sum \Delta\eta_i s_i \quad (2)$$

in the discrete model.  $t^*$  is the travel time,  $t^{\text{pre}}$  is the predicted travel time through the starting model,  $\Delta\eta$  is the slowness perturbation to the starting model,  $S$  is the ray length portion associated with that node determined by a weighted distribution of the four nearest nodes for each ray segment, and  $i$  denotes the particular node. For S waves, the travel time is given by

$$t_s^* = \int \eta_p r \cdot ds, \quad (3)$$

where  $r$  equals Vp/Vs at any point. To build the discrete partial derivative matrix, we use the forward form of

$$t_s^* = t_s^{\text{pre}} + \sum \Delta\eta_i r_i s_i + \sum \eta_i \Delta r_i s_i, \quad (4)$$

where  $\Delta\eta$  and  $\Delta r$  are treated as independent model parameters that affect  $t_s^*$ . This formulation is non-linear in that the partial derivatives assume a prior model. However, because  $\eta, r \gg \Delta\eta, \Delta r$ , minimal returns are gained for further iterations to account for the non-linearity.

[17] The above equation couples the Vp and Vp/Vs inversions, because the S data simultaneously affect both the  $\eta$  and  $r$  parameters. An important note is the difference in magnitude between  $\eta$  and  $r$  (which multiplied by the local path lengths,  $s$ , are the partial derivatives for the S data in the tomography).  $r \sim 1.8$  and  $\eta \sim .102$  for the upper mantle. The relative magnitudes of the partial derivatives are not an issue for a perfectly posed problem. In practice, however, the minimum length solution criterion in conjunction with non-ideal ray coverage allows S residuals to map preferentially into  $\eta$  relative to  $r$ , resulting in weak calculated Vp/Vs anomalies. To account for this disparity, we use a weighting factor,  $\gamma$ , for the Vp/Vs derivatives. This weighting factor is essentially proportional to the a priori ratio of the variance of the model parameters, and accounts for the fact that  $\eta$  is constrained by better than an order of magnitude better than  $r$  in the units used here. The partial derivative matrix and model vector effectively become

$$G = [\partial d_j / \partial \eta_i | \gamma (\partial d_j / \partial r_i)] \quad (5)$$

and

$$m = [\Delta\tau_i|(1/\gamma)\Delta\tau_i]^T, \quad (6)$$

where  $d_j$  refers to the  $j$ th datum and superscript  $T$  denotes transpose. For the tomography presented here, we set  $\gamma$  equal to 24. Greater weighting produces little change in the results, suggesting that this value is about the minimum weight that puts as much emphasis on  $V_p/V_s$  as possible given the model setup.

[18] Hypocenters are relocated prior to each tomographic iteration using a weighted least squares scheme using both local and teleseismic arrivals. Partial derivatives for hypocenter relocation for the local arrivals are given by *Wright and Holt* [1986] using successively updated tomographic velocity models. Teleseismic arrival partial derivatives are found using the AK135 velocity model [*Kennett et al.*, 1995] with travel times corrected for station elevation. Data weights are identical to those discussed above for the tomographic inversion, including the uniform reduction for outliers.

[19] Ray paths are initially traced and events located within a 2-D velocity model assuming a North Fiji Basin velocity structure in the back-arc region above the slab [*Wiens et al.*, 2006]. Below and east of the slab, we assume a Pacific plate velocity structure [*Xu and Wiens*, 1997]. We include an anomaly defined by a 100 km thick slab with an 8% fast maximum anomaly (relative to the North Fiji Basin model) at the slab surface just below the overlying lithosphere that tapers to 4% at 650 km depth and to zero at the base of the slab. The shape and location of the initial slab surface is from *Chen and Brudzinski* [2001]. The initial raytracing must include a seismically fast slab or the non-linearity of the problem drives the solution to a local minimum with the slab anomaly displaced well below the Wadati-Benioff zone [*Zhao et al.*, 1997].

[20] Multidimensional velocity gradients can lead to multipathing of rays near the slab. This effect is noticeable for stations west of the trench for events with sources greater than a few 100 km. We often observe two arrivals with different frequencies and ray parameters at these eastern stations (arrival times are similar near the trench and diverge progressively eastward), with the higher frequency arrival having the greater ray parameter (slower apparent velocity). This behavior suggests that the lower frequency arrival is a direct phase and the higher frequency arrival is from a guided phase in

the slab and Pacific plate. We were unsuccessful at capturing both arrivals with the two-point bending technique, but routinely traced the first arrival. Ideally the tomography would use both arrivals, but for this study we only included the initial arrivals in our data set.

[21] Because both the ray paths and the hypocenter locations depend on the assumed velocity model, ray paths and source locations were iterated as the calculated velocity model was improved. Hypocenters were relocated prior to each of eight successive velocity model inversions. Between hypocenter relocations, iterative tomographic models were calculated by iteratively updating the ray paths twice while keeping the hypocenters fixed. Further iterations for either the ray paths or hypocenter relocations do not significantly decrease the variance. Tests show that the final structure is relatively insensitive to the details and magnitude of the initial slab anomaly.

[22] We include smoothing constraints to help stabilize the inversion. We accomplish this by putting the smoothing constraints directly into the partial derivative matrix before inverting for the tomographic structure. We use a uniformly applied second derivative constraint that depends only on the immediately surrounding nodes [*Menke*, 1984]. We weight the smoothing constraints to maintain as much structure as possible while suppressing large anomaly variations at individual nodes. With the smoothing constraints included directly in the G matrix, the problem becomes nearly overdetermined. Consequently, we use almost all the eigenvectors from the SVD solution. With SVD, the resolution matrix is straightforward to calculate. Figure 5 shows the resolution and spread function [*Toomey and Foulger*, 1989] matrices, neglecting the smoothing constraints. We neglect the smoothing constraints in the resolution and spread matrices, since including the constraints causes the problem to approach the overdetermined case, where the resolution and spread matrices lose meaning. Instead, we prefer to illuminate only the portion of the model space illuminated by actual data. We mask the portions of the tomograms where  $V_p/V_s$  resolution is limited ( $<0.5$ ) (Figure 5). Although the SVD method gives a quantifiable resolution matrix, the resolution solution should be viewed in relative terms rather than absolute, as the uncertainty in and covariance with the hypocenter locations are not reflected in this matrix.

[23] As another measure of the resolution we computed several checkerboard tests with  $\pm 4\%$

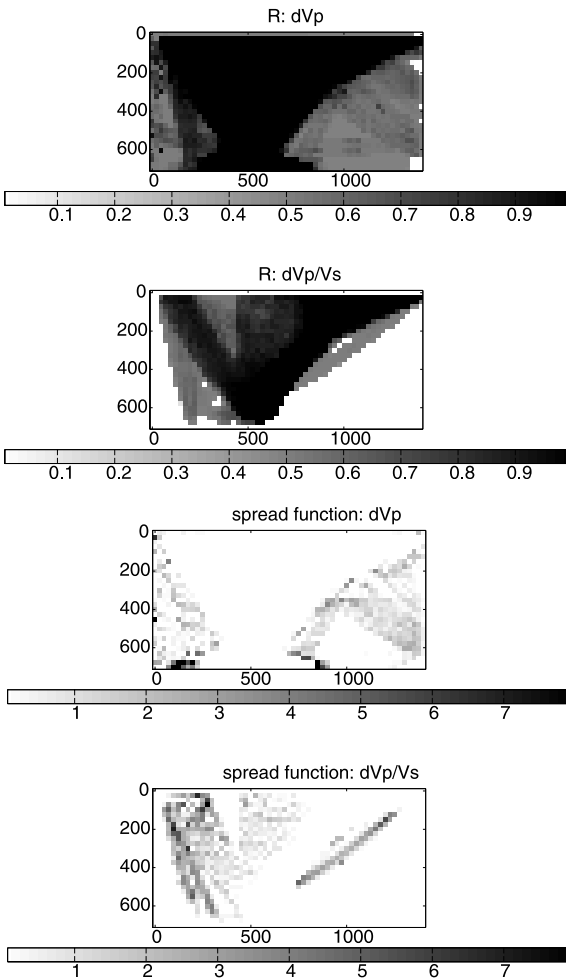


**Figure 5.** Resolution (R) and spread function matrices for Vp, Vp/Vs joint tomography models. Unitless resolution matrices show how well each model parameter is resolved (1 = perfectly resolved; 0 = no resolution), while the spread function gives a measure of smearing effects for each parameter or its covariance with other parameters (off-diagonal elements of the resolution matrix). Covariance between parameters with a greater spatial difference contributes more to the spread. Vp is resolved to a better degree over most of the model space than Vp/Vs because there are more P arrivals than S arrivals, and S arrivals also directly contribute to the Vp solution, while P arrivals only indirectly contribute to the Vp/Vs solution. The best resolved portions of the model space are along the slab, in the back arc between the Lau ridge and the volcanic front, and beneath the Fijian platform.

anomalies relative to our starting model at a few different wavelengths. Although not as quantitative as a formal resolution matrix, such tests give a good visual inspection of the ability of the method to recover certain anomalies. Synthetic travel times are computed through the checkerboard model for

all of our source-receiver pairs. Noise scaled to the standard deviations of the original picks is then added to the travel times and used as data to repeat the inversion process. To examine the covariance among model parameters, we performed separate tests with anomalies only in Vp, only in Vp/Vs, and simultaneously in both Vp and Vp/Vs (Figure 6). The checkerboard tests largely confirm applicability of the resolution matrices, with the best anomaly recovery at all wavelengths occurring in the wedge between the Lau Ridge and the slab, and just beneath Fiji. The Vp and Vp/Vs anomaly recovery is similar whether there are anomalies in only one or both, indicating that the covariance between Vp and Vp/Vs anomalies does not overtly bias the results. In the tests with no synthetic anomaly in one of the variables, recovered anomalies in that variable are typically <0.5%. The recovered checkerboard anomalies are robust at spatial scales down to 100 km or less, but shorter wavelength anomalies are robust over progressively smaller portions of the wedge in both magnitude and spatial extent, with the uppermost corner retaining some resolvability down to 50 km half-wavelengths.

## 4. Results

[24] Each individual iteration, including both the velocity model and hypocenter location, improves the variance by 30% or less. With multiple iterations, our final solution reduces the data variance by more than 70% from the laterally varying starting model. Compared to an initial 1D velocity model, the variance is reduced by more than 90%. Hypocenter relocations are typically <10 km, with a few exceptions that are closer to 30 km. Figures 7 and 8 show our tomography solutions with the least resolved portions masked. Figure 7 shows the calculated anomalies relative to IASP91 [Kennett and Engdahl, 1991]. The seismically fast slab and the broad, slow back-arc anomalies dominate the tomograms. The back-arc anomaly extends to ~200 km depth as is also exhibited in the best fitting 1-D velocity model (Figure 4); a strong slow anomaly in the back arc to depths of ~200 km is expected as the IASP structure model is based largely on continental lithosphere which shows fast velocities at these depths. The back-arc anomaly relative to IASP91 visually dominates the tomograms, so we also plot the anomalies in Figure 8 relative to the best fitting local 1D profile, which is considerably slower than IASP91 in the back arc in both Vp and Vs. Removing the overall back-arc

anomaly highlights the anomalies associated with the arc and spreading center. In the following sections, we will discuss the anomalies relative to the best fitting model for this reason.

#### 4.1. Vp and Vs

[25] Our  $P$  velocity solution (Figure 8a) shows a seismically fast slab and Pacific plate (0.4–0.7 km/s fast) and slow anomalies beneath the arc ( $\sim 0.6$  km/s), CLSC ( $\sim 0.4$  km/s), and Fiji ( $>0.2$  km/s) relative to the best fitting 1D model. The slowest arc and back-arc anomalies are located in the upper 100 km of the mantle, at depths where primary magma production would be expected

[Shen and Forsyth, 1995]. The slow back-arc anomalies extend, at smaller amplitudes (0.1–0.2 km/s), to depths of 300–400 km below the back arc. The deep anomalies beneath the spreading center may be associated with deep dehydration of the slab [Zhao *et al.*, 1997]. The shallow portion of the mantle beneath and west of the Lau Ridge, an extinct island arc, is characterized by much smaller anomalies, suggesting a thicker lithosphere and a structure more similar to average global models.

[26] Most of these features are similar to the  $P$  wave model of Zhao *et al.* [1997], which uses much of the same  $P$ -arrival data. However, some differences between the two studies are present in the details because of differences in the parameterization such as 3D versus 2D, the interplay of  $S$  and  $P$  data in the joint solution, and regularization such as the degree of smoothing and choice of starting model. The most obvious difference is a weaker anomaly beneath the CLSC in our results and a more ambiguous distinction between the arc and CLSC anomalies. Whereas Zhao *et al.* [1997] show their strongest slow anomaly just beneath and west of the CLSC, the CLSC anomaly in our  $V_p$  map is less pronounced and less well defined, especially compared to the arc anomaly. This difference results in part from using a more accurate crustal thickness model in the current results [Crawford *et al.*, 2003], which shows 2–3 km thicker crust to the west of the CLSC relative to the eastern side. However, this difference in crustal thickness accounts for only about 1/3 of the difference between the models. The lack of rays propagating

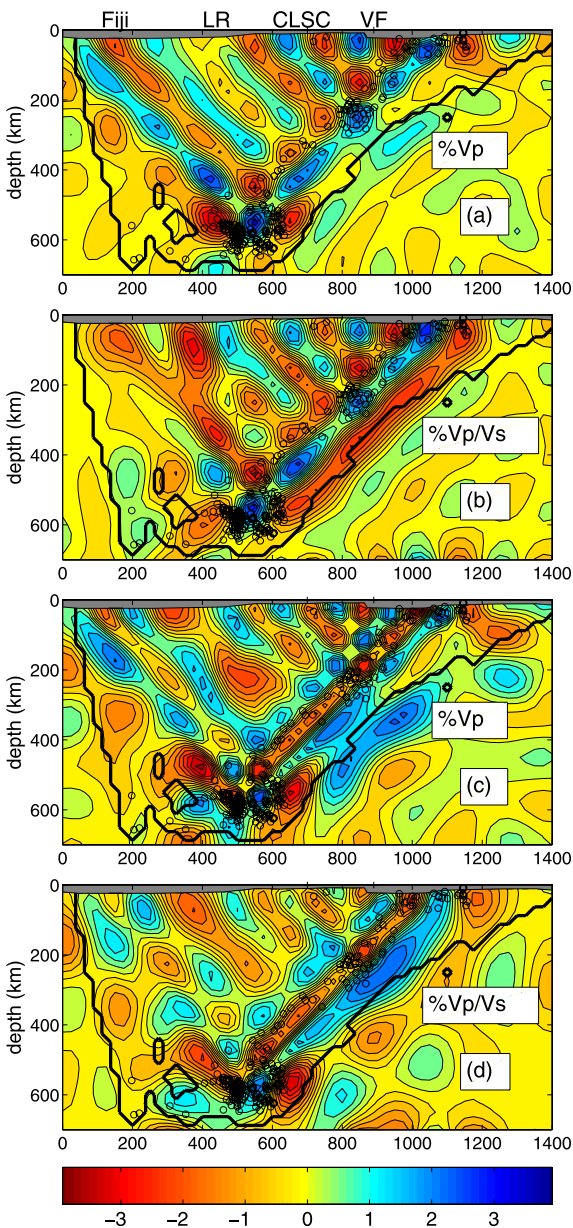


**Figure 6.** Checkerboard resolution tests for the tomography results. Synthetic anomalies of  $\pm 4\%$  were added to the starting model to generate synthetic travel times for all the source-receiver pairs used in the inversion. Noise scaled to the standard deviations of the initial picks was added to the synthetic travel times, which were then used to invert for the structure using the same method outlined in the text. We conducted several tests at differing wavelengths and with the anomalies in one or the other or both  $V_p$  and  $V_p/V_s$ . The dark line denotes the “well-resolved” region as determined by the resolution matrix shown in Figure 5. (a) The recovered  $V_p$  anomalies for a model with anomalies of half-wavelength 100 km and only assumed in  $V_p$ . (b) The recovered  $V_p/V_s$  anomalies for a model with anomalies of half-wavelength 100 km and only assumed in  $V_p/V_s$ . (c) The recovered  $V_p$  anomalies for a model with anomalies of half-wavelength 75 km in both  $V_p$  and  $V_p/V_s$ . (d) The recovered  $V_p/V_s$  anomalies for the same model as Figure 6c.

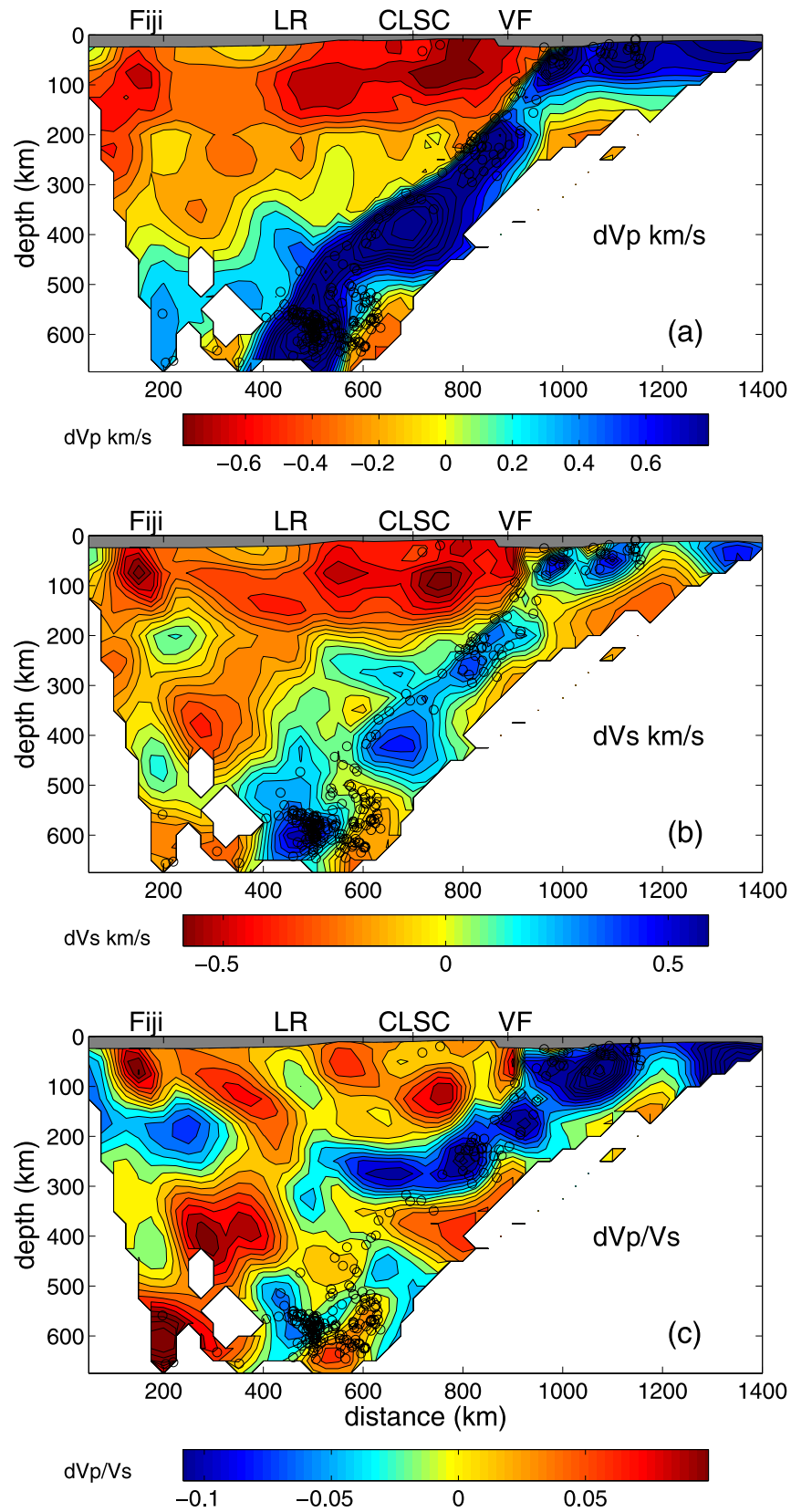


Figure 7

in a north-south direction in the current study may also contribute to this difference.

[27] The  $V_s$  structure (Figure 8b) was not directly solved, but determined by dividing the  $V_p$  solution by the  $V_p/V_s$  solution. Not surprisingly, much of the same character is exhibited in the  $V_s$  structure as the  $V_p$ , but with overall differing magnitudes. In particular, the structure exhibits a fast slab (0.2–0.4 km/s) and a slow arc and spreading center (0.3–0.5 km/s) with several deeper slow anomalies throughout the mantle wedge. Fiji also shows a slow  $V_s$  anomaly (0.4 km/s). The CLSC anomaly is of similar dimension and location to the CLSC  $V_p$  anomaly of *Zhao et al.* [1997], extending >100 km west of the axis, but little to the east. The arc anomaly appears to extend ~150 km west of the volcanic front to ~50 km from the CLSC, while possibly reaching depths >150 km. The proximity of the separate arc and CLSC anomalies in the tomography (and presumably regions of melt production) makes interpretation of the degree of separation between the two anomalies a bit tenuous, but there does appear to be a distinct separation between the anomalies in the  $V_s$  and  $V_p/V_s$  tomograms with the CLSC anomaly almost entirely beneath the west side of the axis. Interpretation that the two melting regimes are distinct is consistent with a lack of melting regime interaction at the CLSC as suggested by petrology [*Taylor and Martinez, 2003*].

#### 4.2. $V_p/V_s$

[28] The resultant  $V_p/V_s$  structure (Figure 8c) highlights many of the features observed on the  $V_p$  and  $V_s$  maps, although the anomalies appear to be somewhat more discontinuous. The anomalies shown are unitless, as they are deviations from initially assumed average  $V_p/V_s$  values for the entire region. There are large positive  $V_p/V_s$  anomalies associated with the arc (~0.05–0.1) and CLSC (~0.1), with the CLSC anomaly appearing to be shifted nearly entirely west of the axis. The CLSC signature in our models (west of the axis) is dominated by the  $S$  wave residuals as the anomaly appears stronger in  $V_p/V_s$  and  $V_s$  than in  $V_p$ . There is also a large  $V_p/V_s$  anomaly in the

shallow mantle beneath the Fiji platform (~0.1). Large negative anomalies are associated with the cold, downgoing slab (0.04–0.1), particularly along the shallower section.

[29] The upper mantle portion of the slab exhibits large negative  $V_p/V_s$  anomalies (~0.1) while the slab anomaly in the transition zone is more subdued. Unexpectedly, there is a large negative  $V_p/V_s$  anomaly at depths of 250–350 km beneath the back-arc basin. We hesitate to directly interpret this feature as it is virtually the only anomaly in these tomograms that is anticorrelated in  $V_p$  and  $V_s$  (slow  $V_p$ , fast  $V_s$ ). There are few known mechanisms for such an anticorrelation, all of which involve complex compositional variations that are far more likely to occur in the lowermost mantle [*Trampert et al., 2004; van der Hilst, 2004*]. This large negative  $V_p/V_s$  wedge anomaly at depths of 250–350 km may partially arise from unaccounted anisotropy in the wedge. Shear wave splitting is stronger (~1s splitting) beneath the Lau Ridge and Fiji plateau than beneath the basin itself [*Smith et al., 2001*]. The large number of rays to Fiji from 200–300 km depth could result in the smearing of fast  $S$  rays into a portion of the model with the fewest crossing rays. However, this hypothesis can account for only 50% of the anomaly magnitude. Another contributing factor may include a systematic error in hypocenter location, but a series of tests with different a priori velocity models producing different initial earthquake locations show virtually no change in the final result. The results may be suggesting at minimum that a significant slow  $V_s$  anomaly does not extend to 300–400 km depth.

#### 4.3. $d\ln V_s/d\ln V_p$

[30]  $d\ln V_s/d\ln V_p$ , often noted as  $\nu$ , is a measure of the relative percentage change of  $V_s$  relative to  $V_p$ . We obtain one measure of  $\nu$  by dividing the change in natural logarithm of the  $V_s$  anomalies by the change in natural log of the  $V_p$  anomalies relative to our best fitting 1D model (Figure 9). The largest values of  $\nu$  (>2) are located in the uppermost 50 km of the mantle directly beneath the volcanic front and west of and below the CLSC. *Nakajima et al.*

**Figure 7.** Final iterated solutions for (a)  $P$  wave velocity anomaly structure ( $V_p$ ), (b)  $S$  wave velocity anomaly structure ( $V_s$ ), and (c)  $V_p/V_s$  anomaly structure. Solutions are determined by a joint  $V_p$  and  $V_p/V_s$  Singular Value Decomposition inversion.  $V_s$  structure is determined by combining the  $V_p$  and  $V_p/V_s$  tomograms. Anomalies are referenced to the IASP91 global velocity model. The solutions are masked where the structures cannot be adequately resolved. Black circles denote hypocenter locations for final iteration. Assumed crustal thickness as determined primarily by seismic refraction [*Crawford et al., 2003*] is shown with gray band at top. Contour intervals are 0.08 km/s for  $V_p$ , 0.06 km/s for  $V_s$ , and 0.012 units for  $V_p/V_s$ .

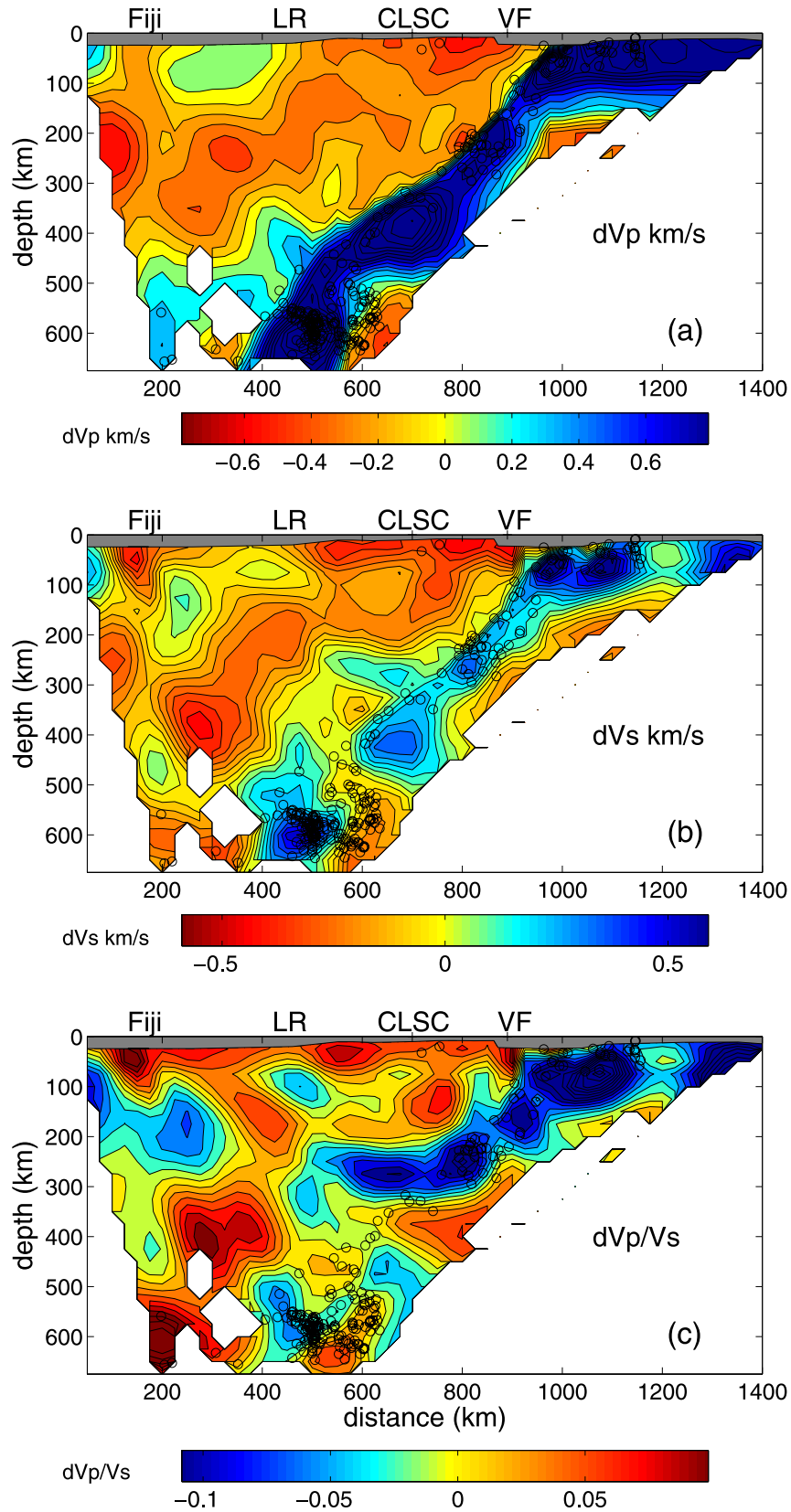
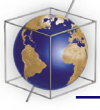
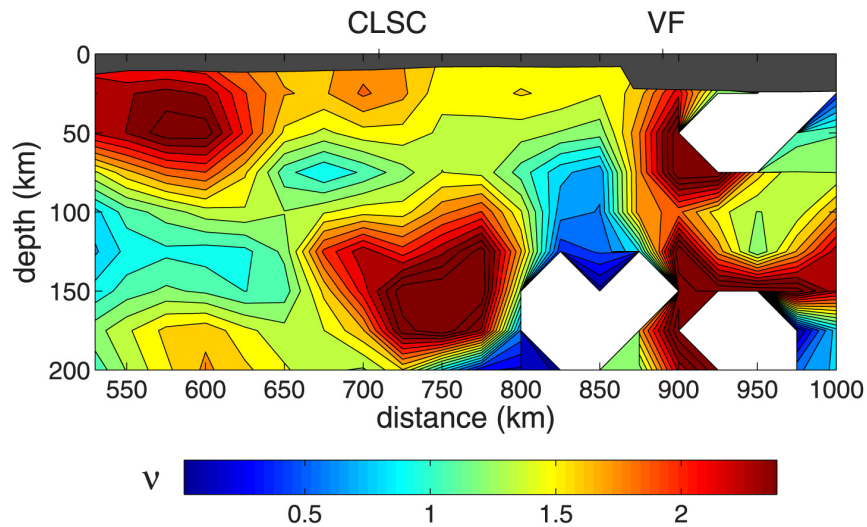


Figure 8



**Figure 9.**  $\ln V_s / \ln V_p$  ( $\nu$ ) in the uppermost mantle of the back arc as measured by dividing the natural log of the  $V_s$  anomalies by the natural log of the  $V_p$  anomalies relative to the best fitting 1D model in Figure 4. Contour interval is 0.14 units. This measure is susceptible to large swings where  $V_p$  and/or  $V_s$  anomalies are small, as evidenced by the two negative (blue) regions shown. For example, the blue spot below the volcanic front (VF) near 100 km depth is the transition region between the seismically fast slab and the seismically slow back arc. Still, some characteristics of the basin are apparent, such as the large ( $>2$ ) values of  $\nu$  from 50 km depth to the top of the mantle beneath the volcanic front and west of and below the CLSC.

[2005] show similar variation in  $\nu$  beneath north-eastern Japan with the highest values ( $>2$ ) between 40–65 km depth beneath the arc and close to unity elsewhere. Although the above measure of  $\nu$  gives a good indication of how  $\nu$  varies throughout the model, it is susceptible to errors of small number arithmetic (where one or both of the anomalies are nearly zero), resulting in a number of spurious values and also gives a measure that is highly dependant on the reference model. So we also present the distribution of  $\nu$  for particular regions of interest by creating histograms of

$$\nu_{ij} = (\ln V_{S_i} - \ln V_{S_j}) / (\ln V_{P_i} - \ln V_{P_j}), \quad (7)$$

where  $i$  and  $j$  denote the nodes within the particular region. This histogram representation allows a model independent assessment of the dominant  $\nu$  signal for a given region.  $\nu$  for our entire model space is close to 1 (Figure 10), but the wedge shows a  $\nu$  dependent on depth. The shallowest portion of the wedge ( $\leq 100$  km) shows a wide

scatter in  $\nu$  values, but has a peak at  $\nu \sim 2.2$  (Figure 10). Extending the region to 200 km depth develops a strong peak near 1.2, but adds little to the peak at 2.2 (Figure 10). Extending the wedge to 400 km depth results in a histogram peaked strongly near 1 and is nearly indistinguishable to that of the entire model. These results suggest that the mantle wedge is characterized by  $\nu$  values that show high values of  $\nu$  ( $\sim 2.2$ ) for some portions of the shallowmost structure (depth  $< 100$  km), with values then rapidly decreasing to near unity with increasing depth. These results generally agree with *Koper et al.* [1999], who found an average mantle wedge  $\nu$  of 1.2–1.3 for ray paths that were dominantly bottoming at depths of 100–200 km beneath the back arc.

[31] We note that either measure of  $\nu$  may be underestimated because of its derivation; i.e., by taking the ratio of two quantities, one of which has previously been determined by a division operation and not directly from the inversion. Along with the other caveats of  $V_s$ , the measure of  $\nu$  is highly susceptible the damping, which tends to make  $\nu$

**Figure 8.** Same as Figure 7, except with the anomalies referenced against the best fitting local 1-D structure (Figure 4). The locally derived 1-D model has a much slower shallow mantle than IASP91 presumably because the upper mantle in the Lau basin is exceptionally warm and IASP91 is biased toward continental structure. Referencing the anomalies against this slower average model highlights other local phenomena, such as the anomalies associated with the arc and CLSC.

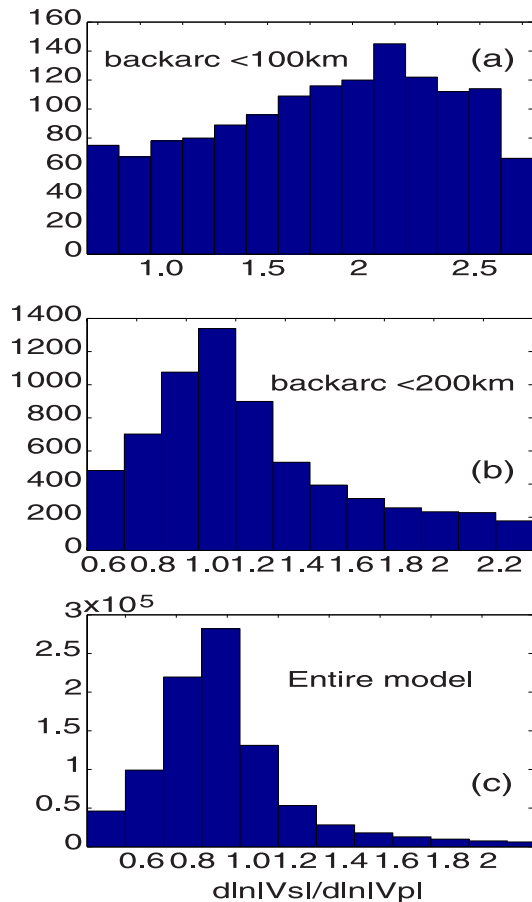


**Figure 10.** Histograms of  $\nu$  determined by the difference in  $\ln|V_s|$  divided by the difference in  $\ln|V_p|$  for all velocity model nodes within a given area. (a) Shallow region ( $\leq 100$  km) beneath the spreading center and arc (horizontal spacing ranges from 425 to 850 km) exhibits a peak around a high value of 2.2, suggesting the presence of high mantle temperatures or melt. (b) Same region as in Figure 10a but extended to 200 km deep shows an immediate change in  $\nu$  to a lower dominant value near 1.2. (c) The entire model space exhibits a value of  $\nu \sim 1$ .

close to 1 where  $V_p/V_s$  is not well constrained by data. Picking  $S_{\text{fast}}$  will also tend to reduce the observed  $\nu$ . However, even as a minimum value, our measures of  $\nu$  imply significant variation in seismic structure within the wedge mantle.

## 5. Discussion

### 5.1. Interpretation of Velocity Anomalies

[32] The velocity anomalies in the mantle wedge result from several possible sources. Increasing temperature, volatile content, and melt fraction will all result in slower seismic velocities [Wiens and

Smith, 2004; Wiens *et al.*, 2006]. Compositional variations have been suggested to cause significant velocity anomalies in the upper mantle, particularly velocity increases with increasing melt extraction through changes in the Fe/Mg ratio [e.g., Jordan, 1979]. However, recent studies suggest that the effect of iron depletion is counteracted by aluminum depletion and that upper mantle velocity should not change substantially as a result of depletion (D. L. Schutt and C. E. Lesher, The effects of melt depletion on the density and seismic velocity of garnet and spinel lherzolite, submitted to *Journal of Geophysical Research*, 2005). Since we have no a priori reason to suspect variable mineralogy throughout the wedge, we do not attempt to interpret any anomalies in terms of compositional variations but in terms of temperature, melt fraction, and volatile content.

[33] Ultrasonic laboratory experiments on single olivine crystals suggest that temperature affects seismic velocities anharmonically in the upper mantle by  $\sim -0.55$  m/s/ $^{\circ}\text{C}$  for  $V_p$  and  $\sim -0.4$  m/s/ $^{\circ}\text{C}$  for  $V_s$  [Anderson *et al.*, 1992; Isaak, 1992], and that anelastic effects in regions such as backarc basins can be of the same order or greater, depending on the seismic attenuation [Karato, 1993]. These results suggest  $\nu$  values of about 1.2 for the anharmonic case. However, since attenuation increases rapidly with temperature [e.g., Jackson *et al.*, 2002] the anelastic effects are non-linear. Recent low-pressure experiments at seismic frequencies show that  $dV_s/dT$  for a grain size of 10 mm more than doubles over the temperature range of 1000 $^{\circ}\text{C}$  to 1450 $^{\circ}\text{C}$ , from  $-0.8$  m/s/ $^{\circ}\text{C}$  to  $-1.7$  m/s/ $^{\circ}\text{C}$ , because of increasing anelasticity [Faul and Jackson, 2005]. Attenuation effects are even greater for smaller grain sizes. As attenuation associated with the bulk modulus is likely to be negligible [Karato and Spetzler, 1990], we can derive an approximation for  $dV_p/dT$  values for temperatures above 1000 $^{\circ}\text{C}$  using the derivatives for shear modulus with temperature, assuming only an anharmonic decrease in bulk modulus with temperature. This relationship gives  $V_p$  derivatives of  $-1.3$  m/s/ $^{\circ}\text{C}$  for 1050 $^{\circ}\text{C}$  and  $-2.0$  m/s/ $^{\circ}\text{C}$  at 1450 $^{\circ}\text{C}$  for the uppermost mantle. These results show that  $\nu$  values can be in the range of 1.5 to 2.0 for seismic body wave frequencies at high temperatures and small grain sizes. Some of the observed shallow anomalies, such as beneath the volcanic arc, reach  $\sim 0.5$  km/s in  $V_p$  and  $>0.4$  km/s in  $V_s$ , requiring perturbations of 300–400 $^{\circ}\text{C}$  or greater if temperature is solely responsible for the anomalies. Clearly,

such mechanisms as partial melt or the presence of fluids could be important as well.

[34] Several studies have investigated how partial melt affects the elastic moduli and therefore seismic velocities [Hammond and Humphreys, 2000; Schmeling, 1985; Takei, 2002], showing that not only the melt fraction, but also the shape distribution of the melt strongly affects the seismic wave speeds. Poro-elastic calculations show that  $d\ln V_s/d\ln V_p$  is sensitive to the pore geometry of the melt and/or fluid phase present in the matrix, whereas the magnitude of the velocity perturbations is an indication of the porosity of the mantle [Takei, 2002]. Hammond and Humphreys [2000] suggest that melt can be identified by values of  $\nu$  near 2 or greater. However, Yoshino *et al.* [2005] suggests the melt geometry used in Hammond and Humphreys [2000] may not be appropriate, and values of  $\nu$  of less than 1.5 can result from an equilibrium melt geometry. It is also clear from Faul and Jackson [2005] that  $\nu$  values of near 2 are possible in the melt-free case for high temperatures and small grain sizes. Faul *et al.* [2004] also show for experiments using melt-containing samples at seismic frequencies that grain-boundary sliding produces a shear modulus reduction that is in addition to the poro-elastic effects noted by other studies [Hammond and Humphreys, 2000; Schmeling, 1985; Takei, 2002]. This shear modulus reduction would affect the  $S$  velocity more than the  $P$  velocity and serve to further increase  $\nu$ . Thus the effect of melt is likely to be substantial shear modulus reduction and high values of  $\nu$ , but the effects of in situ melt in the upper mantle on seismic velocities have not been adequately constrained for a quantitative interpretation of mantle porosity at this point.

## 5.2. Tonga Slab

[35] The slab is seismically fast for both  $V_p$  and  $V_s$  as expected because of the colder temperatures. Koper *et al.* [1999] found  $\nu_{\text{slab}}$  in this region roughly 1.1–1.2 using a set of 11 deep events (therefore no depth resolution). By dividing the natural log of slab  $V_s$  anomalies by the natural log of slab  $V_p$  anomalies, we find  $\nu \sim 1$  over much of the slab length, but somewhat higher (1.3–1.5) for the shallowest portion (100–200 km depth), consistent with the average value determined by their previous study. The slab exhibits fairly weak  $V_p/V_s$  anomalies below 300 km depth. The slab anomaly may be particularly affected by the neglect of anisotropy in the tomography if there fast direction is down (up) dip, because the slab

structure is dominated by ray paths traveling the same direction (up dip) through the slab, unlike most of the back arc with a better proportion of crossing paths (Figure 2). An up dip fast direction would make  $V_s$  appear artificially slow relative to  $V_p$  and could overestimate  $V_p/V_s$  by as much as 0.05 and a corresponding  $V_s$  would appear too slow by as much as  $\sim 0.1$  km/s.

[36] Kennett and Gorbatov [2004] suggest that most slabs exhibit stronger anomalies in shear than in compression, reaching a maximum difference when the subducting slab age is 80–110 Ma (near maximum thickness). While there does seem to be a good correlation for most subduction zones around the Pacific [Kennett and Gorbatov, 2004; Widiyantoro *et al.*, 1999], the Tonga slab seems to be an exception. The subducting seafloor in this region is poorly dated, but certainly older than 110 Ma [Mueller *et al.*, 1997]. Even after accounting for possible anisotropy in the slab, the portion of the slab deeper than 300 km exhibits stronger anomalies in  $V_p$  than in  $V_s$ , particularly in the transition zone. The studies using teleseismic  $P$  and  $S$  travel times have lower resolution, but show a similar structure with bulk sound speed anomalies stronger than shear anomalies for this slab [Gorbatov and Kennett, 2003; Kennett and Gorbatov, 2004], which would predict relatively high  $V_p/V_s$  values. We may speculatively attribute stronger  $V_p$  than  $V_s$  anomalies deeper than 300 km to a reduced rigidity resulting from grain-size reduction associated with phase transformations [Riedel and Karato, 1997; Widiyantoro *et al.*, 1999].

## 5.3. Tonga Arc

[37] The portion of the mantle wedge beneath the volcanic arc exhibits some of the largest slow anomalies in the velocity model, reaching  $>6\%$  in  $V_p$ ,  $>10\%$  in  $V_s$ , and a change of nearly 0.1 in  $V_p/V_s$ . Solely temperature-induced anomalies would require an anomaly of nearly  $400^\circ\text{C}$  relative to the already slow back arc. However, melt and hydration are integral to arc processes, and a  $400^\circ\text{C}$  anomaly at depths of 50–150 km should be well above the peridotite solidus [Hirschmann, 2000], suggesting that melt and/or volatiles are largely responsible for the velocity anomalies. The large  $V_p/V_s$  anomaly also points to melt and hydration playing a significant role beneath the arc.

[38] Given possible extremely low melt fractions implied by rapid extraction times for arc melts [Turner *et al.*, 2000], the slow-velocity anomaly beneath the arc is plausibly derived from the pres-

ence of fluids rather than melt. The anomaly may reach a depth of  $>150$  km as it extends toward the back arc, as was also shown by *Zhao et al.* [1997]. This depth is likely determined by the breakdown of hydrous minerals in the slab at shallow depth, such as serpentine or amphibole [*Fumagalli et al.*, 2001]. The anomaly appears to extend  $\sim 150$  km toward the back arc, further than would be inferred by the distribution of volcanoes at the surface. This suggests that melt migration beneath arcs requires either a focusing mechanism, such as reactive channel development [*Kelemen et al.*, 1995] or coalescing diapirs [*Hall and Kincaid*, 2001], to extract melt at a discrete location some distance from the volcanic front or, that melt is retained in the mantle because the melt geometry is less favorable for rapid migration at a given distance from the volcanic front. Over most of the arc anomaly  $\nu$  is large suggesting a favorable geometry for melt extraction [*Takei*, 2002] (Figure 9), so the arc signal may be primarily a result of hydration. At present, we cannot resolve the porosity magnitude of in situ melt or fluids, but the tomograms likely delineate the respective melt production regions. Undoubtedly, some melt or hydration is present beneath the arc. However, as the experimental data and theoretical considerations suggest large effects on attenuation (and subsequently velocity) with melt and/or fluids, only a small degree of melt (likely substantially  $<1\%$ ) or hydration may be necessary to produce the observed anomalies.

#### 5.4. Central Lau Spreading Center

[39] Melt generation at spreading centers could be a passive process associated with decompression during plate separation [*Phipps Morgan*, 1987] or could be an active process as buoyant melt drives convection in a narrow region beneath the axis [*Buck and Su*, 1989]. Whether one process dominates over the other may depend on spreading rate or other factors such as the viscosity of the mantle [*Parmentier and Phipps Morgan*, 1990]. Seismic results from the East Pacific Rise (EPR) show a broad zone of melting, consistent with a passive melt generation mechanism [*Forsyth et al.*, 1998; *Hung and Forsyth*, 2000]. Although the CLSC is a fast spreading center like the EPR, the somewhat slower spreading rate (9 cm/yr instead of 14.5 cm/yr) [*Zellmer and Taylor*, 2001] and the back-arc nature of the CLSC imply the possibility of more complex geodynamic behaviors that could result in an active upwelling pattern beneath the axis [*Jurdy and Stefanick*, 1983; *Ribe*, 1989]. The CLSC anomaly extends over a wide region ( $\sim 150$  km

to the west of the axis, and to a limited extent to the east. Such a broad anomaly suggests a passive plate separation melting mechanism dominates at fast spreading centers, even in the more complex back-arc environment.

[40] While the arc anomaly seems to deepen as it approaches the back arc, the CLSC anomaly appears to remain shallower than 70 km to the west of the axis. The CLSC shows large velocity anomalies in  $V_p$  (0.2–0.4 km/s),  $V_s$  (0.3–0.4 km/s), and  $V_p/V_s$  (0.06–0.1), with  $\nu > 2$  (Figures 9 and 10). These anomalies are comparable to the largest anomalies observed on the EPR [*Gu et al.*, 2005]. The CLSC anomaly magnitudes are too large to easily explain solely by thermal variations, even for a grain size of  $\sim 1$  mm [*Faul and Jackson*, 2005]. In addition, it may be difficult to reach  $\nu > 2$  without a small degree of melt or fluid present or submillimeter scale grain size [*Faul and Jackson*, 2005; *Takei*, 2002]. However, it probably retains no more melt than inferred for the EPR ( $<0.5\%$ ) [*Hammond and Toomey*, 2003; *Gu et al.*, 2005]. So, while the  $V_p$  anomaly associated with the CLSC is somewhat ambiguous, the significant  $V_p/V_s$  anomaly beneath the CLSC is well defined and likely defines the primary region of melt production associated with the spreading center.

[41] The spatial distribution of the melt production regions of the CLSC (and arc) has important implications regarding mantle geodynamics of the back arc. Mantle flow driven primarily by plate separation would result in a primarily symmetric upwelling structure beneath the axis [e.g., *Phipps Morgan*, 1987] and shallow, symmetric anomalies. The same may be true of upwelling driven primarily by diapirism beneath the axis, although the depth extent is more uncertain. Given the asymmetry of the CLSC anomaly, the complex mantle dynamics in this back-arc region likely modifies the upwelling driven by plate separation with a component of across-axis mantle flow [*Conder et al.*, 2002a, 2002b]. We note that although the anomaly is shifted significantly westward away from the trench, it does not imply the absence of north-south flow as inferred by geochemical [*Turner and Hawkesworth*, 1998] or shear wave splitting studies [*Fischer et al.*, 2000; *Smith et al.*, 2001], but rather that there must be a significant component of subduction related corner flow 400 km away from the trench.

#### 5.5. Mantle Wedge

[42] Between 200–400 km depth, the tomograms exhibit moderate anomalies in  $V_p$ ,  $V_s$ , and  $V_p/V_s$ .

The largest arc associated anomalies appear to extend to 150–200 km depth. This may mark the depth of primary dehydration of the slab. The proximity of these anomalies at 150–200 km depth to both the volcanic front and the CLSC leaves the possibility of interaction with the CLSC. However, such interaction is probably minimal as the petrology and other geophysical signatures of the CLSC show little affinity for arc melts [Martinez and Taylor, 2002; Taylor and Martinez, 2003]. Deeper, weaker anomalies throughout the wedge may indicate weak, continuous hydration continuing below 200 km, as those extending to 300 km beneath the spreading center may result from a small amount of continuous hydration from the subducting slab [Poli and Schmidt, 1995; Schmidt and Poli, 1998; Zhao et al., 1997]. Conversely, these anomalies could also be accounted for by moderate temperature perturbations, which may be supported by the absence of significant slow Vs anomalies above the slab at depths >250 km.

[43] Most of the wedge exhibits a  $\nu \sim 1$  (Figure 10), consistent with temperature as the primary mechanism for velocity perturbations below 350 km. However, the one localized anomaly at 400 km depth below the Lau Ridge is somewhat higher (1.5–2) when examined in isolation. Hydrated mantle could account for such a signature, as the anomaly is quite weak in Vp (<0.1 km/s), while the dVp/Vs anomaly is much stronger ( $\sim 0.4$ ) and hydration from the subducting slab could be punctuated in places [Tatsumi, 1989] as well as continuous with the breakdown at depth of phengite or topaz-OH in the sediments [Ono, 1998], or lawsonite in the MORB crust [Ono, 1998; Poli and Schmidt, 2002]. If this anomaly is the result of slab dehydration, it may not have come from the Tonga slab as this anomaly is >100 km away from the Tonga slab with a fast Vs anomaly between. However, subduction was occurring beneath the Lau Ridge at 5 Ma [Cole et al., 1990], and the Vitiaz slab was subducting from the north as recently as 2 Ma [Sinton et al., 1985; Pelletier et al., 1996]. With the complex subduction history in this region, other sources may account for deep hydration beneath the Lau Ridge. It is also likely that Indian mantle influxes into the Lau Basin [Hergt and Hawkesworth, 1994; Pearce et al., 1995], so it may be that this anomaly is a hydrated region or region with preferentially small grain size of influxing Indian mantle. Although, it is also not obvious why incoming Indian mantle would contain such a heterogeneity.

## 5.6. Fiji

[44] Seismic velocities are faster beneath the Lau Ridge compared to elsewhere in the back arc (Figure 8). These faster velocities likely indicate a thicker lithosphere, which did not undergo much extension during rifting of the basin. The slow-velocity anomalies and large Vp/Vs anomaly associated with the Fiji plateau indicating thinner lithosphere than beneath the Lau ridge and the possibility of magmagenesis.

[45] Extensional faulting has occurred and is presently occurring on the Fiji platform [Hamburger et al., 1988, 1990]. Volcanism in Fiji began in the upper Eocene ( $\sim 40$  Ma) and has continued to the recent past [Colley and Hindle, 1984; Gill et al., 1984]. Most of Viti Levu (the largest Fijian island) was emplaced prior to 6 Ma, with the more recent, but less voluminous volcanic deposits occurring away from Viti Levu on the Lau islands, Koro, Kadavu, and Taveuni [Colley and Hindle, 1984], with the most recent documented eruption at  $\sim 2000$  BP in Taveuni [Cole et al., 1990]. While we include the station at Kadavu, the stations on Viti Levu dominate the ray coverage to Fiji, so the anomaly seems to be associated with the main Fijian island rather than the outer islands.

[46] Although unexpected, the large Vp/Vs anomaly beneath Fiji is large enough to suggest high temperatures and possible melt production in the shallow mantle. Explanations for melt production beneath Fiji remain speculative, with the variable petrology observed in recent (<3 Myr) volcanism indicating a complexity of melting mechanisms [Gill et al., 1984]. It may be possible that upwelling beneath the extended lithosphere has triggered a small amount of melting beneath the platform. The true dimensions of this anomaly are poorly defined in our tomograms, primarily because all the arrivals come from the east or directly beneath Fiji. However, its presence appears robust, as this region is a fairly well resolved portion of the model with crossing rays to Viti Levu having a reasonable distribution of incidence angles between  $0^\circ$  and  $90^\circ$  (Figure 5).

## 6. Summary

[47] The Lau Basin is a geologically dynamic region with arc volcanism, back-arc spreading and volatile migration occurring within the mantle wedge. Using joint Vp, Vp/Vs tomography, we illuminate wedge structure linked to processes that control the dynamics and geological history of the

Lau Basin. Nearly all key geophysical processes responsible for the observed seismic anomalies in the Basin are influenced by the subducting Pacific plate. The Pacific plate itself is old, thick, and cold with a fast seismic signature for both  $P$  and  $S$  wave velocities. The slab appears to release a significant amount of volatiles to a depth of 150–200 km inducing the arc volcanism observed along the Tofua arc (active western edge of the Tonga arc). The arc anomaly is strong immediately beneath the arc front, and extends westward and deeper toward the back arc. Continued wedge hydration may continue to 300 km depth or more at a lesser rate, with a possible surge because of the complete breakdown of one or more hydrous minerals near that depth.

[48] The CLSC melting region is likely distinct from the arc melting region at this spacing. The slow anomaly associated with the CLSC is broad, extending  $\sim 150$  km to the west, suggesting that melting at the CLSC is passively driven by spreading of the lithosphere. The distribution of larger  $\nu$  values to the west of the axis relative to the east, coupled with the petrology and other geophysical factors [Martinez and Taylor, 2002], suggest that a strong asymmetry is likely and that the anomaly east of the axis is probably associated with the arc. If the melt production region is asymmetric about the axis, the asymmetry probably results from a significant corner flow in the wedge induced from the downgoing slab [Conder et al., 2002a]. If the asymmetry is less, the degree of interaction between the arc and spreading center melt regions could be greater at this spacing than is presently assumed. A component of north-south flow in the wedge could also be present, but cannot be determined from our east-west cross section.

[49] Although the primary signature beneath the Lau ridge is consistent with thicker lithosphere than the adjacent basin, the seismic signature beneath Fiji suggests a thinner lithosphere and warmer mantle temperatures. Partial melt beneath Fiji may be triggered by upwelling beneath a thinned lithosphere.

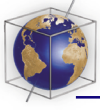
## Acknowledgments

[50] We thank Gideon Smith, Rob Dunn, and Uli Faul for thoughtful comments and discussions. Bill Menke suggested the joint inverse procedure we used. We thank Leroy Dorman, Paul Friberg, John Hildebrand, Patrick Shore, and Spahr Webb for assistance in collecting the original data during the SPASE, LABATTS, and SAFT projects and Keith Koper and Dapeng Zhao for previous work with parts of this arrival time database.

Andrew Goodliffe provided the locations for the neovolcanic zone delineated in Figure 1. Yu Jeffery Gu and an anonymous reviewer provided useful and insightful comments that improved the quality of this manuscript. This research was supported by National Science Foundation grants OCE-0002527, EAR-0001158, and OCE-0305292.

## References

- Aggarwal, Y. P., M. Barazangi, and B. Isacks (1972),  $P$  and  $S$  travel times in the Tonga-Fiji region: A zone of low-velocity in the uppermost mantle behind the Tonga Island Arc, *J. Geophys. Res.*, *77*(32), 6427–6434.
- Anderson, O. L., D. Isaak, and H. Oda (1992), High-temperature elastic constant data on mineral relevant to geophysics, *Rev. Geophys.*, *30*, 57–90.
- Barazangi, M., B. L. Isacks, J. Oliver, J. Dubois, and G. Pascal (1973), Descent of lithosphere beneath New Hebrides, Tonga-Fiji and New Zealand: Evidence for detached slabs, *Nature*, *242*(5393), 98–101.
- Bevis, M., D. A. Phillips, F. W. Taylor, J. Beavan, E. Kendrick, D. Matheson, and B. Schutz (2000), Revised estimates of crustal velocity in the Tonga-Lau System, *Eos Trans. AGU*, Fall Meet. Suppl., *81*(48), Abstract G11A-18.
- Buck, R., and W. Su (1989), Focused mantle upwelling below mid-ocean ridges due to feedback between viscosity and melting, *Geophys. Res. Lett.*, *16*, 641–644.
- Cameron, B. I., J. A. Walker, M. J. Carr, L. C. Patino, O. Matias, and M. D. Feigenson (2003), Flux versus decompression melting at stratovolcanoes in southeastern Guatemala, *J. Volcanol. Geotherm. Res.*, *119*(1–4), 21–50.
- Chen, W.-P., and M. R. Brudzinski (2001), Evidence for a large-scale remnant of subducted lithosphere beneath Fiji, *Science*, *292*(5526), 2475–2479.
- Chiarabba, C., and A. Amato (2003),  $V_p$  and  $V_p/V_s$  images in the  $M_w$  6.0 Colfiorito fault region (central Italy): A contribution to the understanding of seismotectonic and seismogenic processes, *J. Geophys. Res.*, *108*(B5), 2248, doi:10.1029/2001JB001665.
- Cole, J. W., I. J. Graham, and I. L. Gibson (1990), Magmatic evolution of late Cenozoic volcanic rocks of the Lau Ridge, Fiji, *Contrib. Mineral. Petrol.*, *104*(5), 540–554.
- Colley, H., and W. H. Hindle (1984), Volcano-tectonic evolution of Fiji and adjoining marginal basins, in *Marginal Basin Geology*, edited by B. P. Kokelaar and M. F. Howells, *Geol. Soc. Spec. Publ.*, *16*, 151–162.
- Conder, J. A. (2005), A case for hot slab surface temperatures in numerical viscous flow models of subduction zones with an improved fault zone parameterization, *Phys. Earth Planet. Inter.*, *149*, 155–164.
- Conder, J. A., D. A. Wiens, and J. Morris (2002a), On the decompression melting structure at volcanic arcs and back-arc spreading centers, *Geophys. Res. Lett.*, *29*(15), 1727, doi:10.1029/2002GL015390.
- Conder, J. A., D. W. Forsyth, and E. M. Parmentier (2002b), Asthenospheric flow and asymmetry of the East Pacific Rise, MELT area, *J. Geophys. Res.*, *107*(B12), 2344, doi:10.1029/2001JB000807.
- Crawford, W. C., J. A. Hildebrand, L. M. Dorman, S. C. Webb, and D. A. Wiens (2003), Tonga Ridge and Lau Basin crustal structure from seismic refraction data, *J. Geophys. Res.*, *108*(B4), 2195, doi:10.1029/2001JB001435.
- Enguchi, T., Y. Fujinawa, and M. Ukawa (1989), Microearthquakes and tectonics in an active back-arc basin; the Lau Basin, *Phys. Earth Planet. Inter.*, *56*(3–4), 210–229.



- Faul, U. H., and I. Jackson (2005), The seismological signature of temperature and grain size variations in the Upper Mantle, *Earth Planet. Sci. Lett.*, *234*, 119–134.
- Faul, U. H., J. D. Fitz Gerald, and I. Jackson (2004), Shear wave attenuation and dispersion in melt-bearing olivine polycrystals: 2. Microstructural interpretation and seismological implications, *J. Geophys. Res.*, *109*, B06202, doi:10.1029/2003JB002407.
- Fischer, K. M., E. M. Parmentier, A. R. Stine, and E. R. Wolfe (2000), Modeling anisotropy and plate-driven flow in the Tonga subduction zone back arc, *J. Geophys. Res.*, *105*, 16,181–16,191.
- Forsyth, D. W., et al. (1998), Imaging the deep seismic structure beneath a mid-ocean ridge: The MELT experiment, *Science*, *280*(5367), 1215–1218.
- Fujiwara, T., T. Yamazaki, and M. Joshima (2001), Bathymetry and magnetic anomalies in the Havre Trough and southern Lau Basin: From rifting to spreading in back-arc basins, *Earth Planet. Sci. Lett.*, *185*(3–4), 253–264.
- Fumagalli, P., L. Stixrude, S. Poli, and D. Snyder (2001), The 10A phase: A high-pressure expandable sheet silicate stable during subduction of hydrated lithosphere, *Earth Planet. Sci. Lett.*, *186*(2), 125–141.
- Gill, J. B., A. L. Stork, and P. M. Whelan (1984), Volcanism accompanying back-arc basin development in the southwest Pacific, *Tectonophysics*, *102*, 207–224.
- Gorbatov, A., and B. L. N. Kennett (2003), Joint bulk-sound and shear tomography for western Pacific subduction zones, *Earth Planet. Sci. Lett.*, *210*(3–4), 527–543.
- Gu, Y. J., S. C. Webb, A. Lerner-Lam, and J. B. Gaherty (2005), Upper mantle structure beneath the eastern Pacific Ocean ridges, *J. Geophys. Res.*, *110*, B06305, doi:10.1029/2004JB003381.
- Hall, P. S., and C. Kincaid (2001), Diapiric flow at subduction zones: A recipe for rapid transport, *Science*, *292*(5526), 2472–2475.
- Hamburger, M. W., and B. L. Isacks (1987), Deep earthquakes in the Southwest Pacific: A tectonic interpretation, *J. Geophys. Res.*, *92*(13), 13,841–13,854.
- Hamburger, M. W., I. B. Everingham, B. L. Isacks, and M. Barazangi (1988), Active tectonism with the Fiji Platform, Southwest Pacific, *Geology*, *16*(3), 237–241.
- Hamburger, M. W., I. B. Everingham, B. L. Isacks, and M. Barazangi (1990), Seismicity and crustal structure of the Fiji Platform, Southwest Pacific, *J. Geophys. Res.*, *95*(3), 2553–2573.
- Hammond, W. C., and E. D. Humphreys (2000), Upper mantle seismic wave velocity: Effects of realistic partial melt geometries, *J. Geophys. Res.*, *105*, 10,975–10,986.
- Hammond, W. C., and D. R. Toomey (2003), Seismic velocity anisotropy and heterogeneity beneath the Mantle Electromagnetic and Tomography Experiment (MELT) region of the East Pacific Rise from analysis of *P* and *S* body waves, *J. Geophys. Res.*, *108*(B4), 2176, doi:10.1029/2002JB001789.
- Hergt, J. M., and C. J. Hawkesworth (1994), Pb-, Sr-, and Nd-isotopic evolution of the Lau Basin; implications for mantle dynamics during backarc opening, *Proc. Ocean Drill. Program Sci. Results*, *135*, 505–517.
- Hirschmann, M. M. (2000), Mantle solidus: Experimental constraints and the effects of peridotite composition, *Geochem. Geophys. Geosyst.*, *1*(10), doi:10.1029/2000GC000070.
- Hung, S.-H., and D. W. Forsyth (2000), Can a narrow, melt-rich, low-velocity zone of mantle upwelling be hidden beneath the East Pacific Rise? Limits from waveform modeling and the MELT experiment, *J. Geophys. Res.*, *105*, 7945–7960.
- Isaak, D. G. (1992), High-temperature elasticity of iron-bearing olivines, *J. Geophys. Res.*, *97*(B2), 1871–1885.
- Isacks, B., L. R. Sykes, and J. Oliver (1969), Focal mechanisms of deep and shallow earthquakes in the Tonga-Kermadec region and the tectonics of island arcs, *Geol. Soc. Am. Bull.*, *80*(8), 1443–1469.
- Jackson, I., J. D. Fitz Gerald, U. H. Faul, and B. H. Tan (2002), Grain-size-sensitive seismic wave attenuation in polycrystalline olivine, *J. Geophys. Res.*, *107*(B12), 2360, doi:10.1029/2001JB001225.
- Jeffreys, H. (1932), An alternative to the rejection of observations, *Proc. R. Soc. London, Ser. A*, *137*, 78–87.
- Johnson, M. C., and T. Plank (1999), Dehydration and melting experiments constrain the fate of subducted sediments, *Geochem. Geophys. Geosyst.*, *1*(1), doi:10.1029/1999GC000014.
- Jordan, T. H. (1979), Mineralogies, densities, and seismic velocities of garnet lherzolites and their geophysical implications, in *The Mantle Sample: Inclusions in Kimberlites and Other Volcanics: Proceedings of the 2nd International Kimberlite Conference*, vol. 2, edited by F. R. Boyd et al., pp. 1–14, AGU, Washington, D.C.
- Jurdy, D. M., and M. Stefanick (1983), Flow models for back-arc spreading, *Tectonophysics*, *99*, 191–206.
- Karato, S. (1993), Importance of anelasticity in the interpretation of seismic tomography, *Geophys. Res. Lett.*, *20*, 1623–1626.
- Karato, S., and H. A. Spetzler (1990), Defect microdynamics in minerals and solid-state mechanisms of seismic wave attenuation and velocity dispersion in the mantle, *Rev. Geophys.*, *28*, 399–421.
- Karig, D. E. (1971), Origin and development of marginal basins in the western Pacific, *J. Geophys. Res.*, *76*, 2542–2561.
- Kelemen, P. B., J. A. Whitehead, E. Aharonov, and K. A. Jordahl (1995), Experiments on flow focusing in soluble porous media, with applications to melt extraction from the mantle, *J. Geophys. Res.*, *100*(1), 475–496.
- Kennett, B. L. N., and E. R. Engdahl (1991), Travel times for global earthquake location and phase identification, *Geophys. J. Int.*, *105*(2), 429–465.
- Kennett, B. L. N., and A. Gorbatov (2004), Seismic heterogeneity in the mantle: Strong shear wave signature of slabs from joint tomography, *Phys. Earth Planet. Inter.*, *146*, 87–100.
- Kennett, B. L. N., E. R. Engdahl, and R. Buland (1995), Constraints on seismic velocities in the Earth from travel times, *Geophys. J. Int.*, *122*(1), 108–124.
- Kolobov, V. Y., I. Y. Kulakov, and Y. V. Tikunov (2003), Deep structure and geodynamic evolution of the Tonga-New Hebrides region from seismic tomography data, *Geotectonics*, *37*(2), 151–160.
- Koper, K. D., D. A. Wiens, L. Dorman, J. Hildebrand, and S. Webb (1999), Constraints on the origin of slab and mantle wedge anomalies in Tonga from the ratio of *S* to *P* velocities, *J. Geophys. Res.*, *104*(7), 15,089–15,104.
- Martinez, F., and B. Taylor (2002), Mantle wedge control on back-arc crustal accretion, *Nature*, *416*, 417–420.
- Menke, W. (1984), *Geophysical Data Analysis: Discrete Inverse Theory*, 260 pp., Elsevier, New York.
- Mueller, R. D., W. R. Roest, J.-Y. Royer, L. M. Gahagan, and J. G. Sclater (1997), Digital isochrons of the world's ocean floor, *J. Geophys. Res.*, *102*(2), 3211–3214.
- Nakajima, J., T. Matsuzawa, A. Hasegawa, and D. Zhao (2001), Three-dimensional structure of  $V_p$ ,  $V_s$ , and  $V_p/V_s$  beneath northeastern Japan: Implications for arc magmatism and fluids, *J. Geophys. Res.*, *106*(B10), 21,843–21,858.

- Nakajima, J., Y. Takei, and A. Hasegawa (2005), Quantitative analysis of the inclined low-velocity zone in the mantle wedge of northeastern Japan: A systematic change of melt-filled pore shapes with depth and its implications for melt migration, *Earth Planet. Sci. Lett.*, *234*, 59–70.
- Nakamura, M., Y. Yoshida, D. Zhao, H. Katao, and S. Nishimura (2003), Three-dimensional P- and S-wave velocity structures beneath the Ryukyu Arc, *Tectonophysics*, *369*, 121–143.
- Ono, S. (1998), Stability limits of hydrous minerals in sediment and mid-ocean ridge basalt compositions; implications for water transport in subduction zones, *J. Geophys. Res.*, *103*(8), 18,253–18,267.
- Parmentier, E. M., and J. Phipps Morgan (1990), Spreading rate dependence of three-dimensional structure in oceanic spreading centres, *Nature*, *348*(6299), 325–328.
- Parson, L. M., and J. W. Hawkins (1994), Two-stage ridge propagation and the geological history of the Lau backarc basin, *Proc. Ocean Drill. Program Sci. Results*, *135*, 819–828.
- Pearce, J. A., M. Ernewein, S. H. Bloomer, L. M. Parson, B. J. Murton, and L. E. Johnson (1995), Geochemistry of Lau Basin volcanic rocks: Influence of ridge segmentation and arc proximity, in *Volcanism Associated With Extension at Consuming Plate Margins*, edited by J. L. Smellie, *Geol. Soc. Spec. Publ.*, *81*, 53–75.
- Pelletier, B., J.-M. Auzende, and J.-Y. Collot (1996), Geometry and structure of the Vitiaz Trench lineament (SW Pacific), *Mar. Geophys. Res.*, *18*, 305–335.
- Pelletier, B., Y. Lagabriele, M. Benoit, G. Cabioch, S. Calmant, E. Garel, and C. Guivel (2001), Newly identified segments of the Pacific-Australia plate boundary along the North Fiji transform zone, *Earth Planet. Sci. Lett.*, *193*(3–4), 347–358.
- Phipps Morgan, J. (1987), Melt migration beneath mid-ocean spreading centers, *Geophys. Res. Lett.*, *14*(12), 1238–1241.
- Poli, S., and M. W. Schmidt (1995), H<sub>2</sub>O transport and release in subduction zones: Experimental constraints on basaltic and andesitic systems, *J. Geophys. Res.*, *100*(11), 22,299–22,314.
- Poli, S., and M. W. Schmidt (2002), Petrology of subducted slabs, *Annu. Rev. Earth Planet. Sci.*, *30*, 207–235.
- Ribe, N. M. (1989), Mantle flow induced by back arc spreading, *Geophys. J. Int.*, *98*, 85–91.
- Riedel, M. R., and S.-i. Karato (1997), Grain-size evolution in subducted oceanic lithosphere associated with the olivine-spinel transformation and its effects on rheology, *Earth Planet. Sci. Lett.*, *148*(1–2), 27–43.
- Roggensack, K., R. L. Hervig, S. B. McKnight, and S. N. Williams (1997), Explosive basaltic volcanism from Cerro Negro Volcano; influence of volatiles on eruptive style, *Science*, *277*(5332), 1639–1642.
- Roth, E. G., D. A. Wiens, L. M. Dorman, J. Hildebrand, and S. C. Webb (1999), Seismic attenuation tomography of the Tonga-Fiji region using phase pair methods, *J. Geophys. Res.*, *104*, 4795–4810.
- Schmeling, H. (1985), Numerical models on the influence of partial melt on elastic, anelastic and electric properties of rocks: Part 1, Elasticity and anelasticity, *Phys. Earth Planet. Inter.*, *41*(1), 34–57.
- Schmidt, M. W., and S. Poli (1998), Experimentally based water budgets for dehydrating slabs and consequences for arc magma generation, *Earth Planet. Sci. Lett.*, *163*(1–4), 361–379.
- Shen, Y., and D. W. Forsyth (1995), Geochemical constraints on initial and final depths of melting beneath mid-ocean ridges, *J. Geophys. Res.*, *100*, 2211–2237.
- Sinton, J. M., K. T. M. Johnson, R. C. Price, and T. M. Brocher (1985), Petrology and geochemistry of volcanic rocks from the Northern Melanesian Borderland, in *Investigations of the Northern Melanesian Borderland*, *Earth Sci. Ser.*, vol. 3, edited by T. M. Brocher, pp. 35–65, Circum-Pac. Council for Energy and Miner. Resour., Houston, Tex.
- Sisson, T. W., and S. Bronto (1998), Evidence for pressure-release melting beneath magmatic arcs from basalt at Galunggung, Indonesia, *Nature*, *391*, 883–886.
- Smith, G. P., D. A. Wiens, K. M. Fischer, L. M. Dorman, S. C. Webb, and J. A. Hildebrand (2001), A complex pattern of mantle flow in the Lau backarc, *Science*, *292*, 713–716.
- Smith, W. H. F., and D. T. Sandwell (1997), Global sea floor topography from satellite altimetry and ship depth soundings, *Science*, *277*(5334), 1956–1962.
- Sykes, L. R., B. L. Isacks, and J. Oliver (1969), Spatial distribution of deep and shallow earthquakes of small magnitudes in the Fiji-Tonga region, *Bull. Seismol. Soc. Am.*, *59*(3), 1093–1113.
- Takei, Y. (2002), Effect of pore geometry on  $V_p/V_s$ : From equilibrium geometry to crack, *J. Geophys. Res.*, *107*(B2), 2043, doi:10.1029/2001JB000522.
- Tatsumi, Y. (1989), Migration of fluid phases and genesis of basalt magmas in subduction zones, *J. Geophys. Res.*, *94*(4), 4697–4707.
- Taylor, B., and F. Martinez (2003), Back-arc basin basalt systematics, *Earth Planet. Sci. Lett.*, *210*(3–4), 481–497.
- Taylor, B., K. Zellmer, F. Martinez, and A. M. Goodliffe (1996), Sea-floor spreading in the Lau back-arc basin, *Earth Planet. Sci. Lett.*, *144*(1–2), 35–40.
- Tibi, R., and D. A. Wiens (2005), Detailed structure and sharpness of upper mantle discontinuities in the Tonga subduction zone from regional broadband arrays, *J. Geophys. Res.*, *110*, B06313, doi:10.1029/2004JB003433.
- Toomey, D. R., and G. R. Foulger (1989), Tomographic inversion of local earthquake data from the Hengill-Grensdalur central volcano complex, Iceland, *J. Geophys. Res.*, *94*, 17,497–17,510.
- Trampert, J., F. Deschamps, J. Resovsky, and D. Yuen (2004), Probabilistic tomography maps chemical heterogeneities throughout the lower mantle, *Science*, *306*, 853–856.
- Turner, S., B. Bourdon, C. Hawkesworth, and P. Evans (2000), <sup>226</sup>Ra-<sup>230</sup>Th evidence for multiple dehydration events, rapid melt ascent and the time scales of differentiation beneath the Tonga-Kermadec island arc, *Earth Planet. Sci. Lett.*, *179*(3–4), 581–593.
- Turner, S., and C. Hawkesworth (1998), Using geochemistry to map mantle flow beneath the Lau Basin, *Geology*, *26*(11), 1019–1022.
- Um, J., and C. H. Thurber (1987), A fast algorithm for two-point seismic ray tracing, *Bull. Seismol. Soc. Am.*, *77*(3), 972–986.
- van der Hilst, R. (1995), Complex morphology of subducted lithosphere in the mantle beneath the Tonga Trench, *Nature*, *374*(6518), 154–157.
- van der Hilst, R. (2004), Changing views on Earth's deep mantle, *Science*, *306*, 817–818.
- Walck, M. C. (1988), Three-dimensional Vp/Vs variations for the Coso region, California, *J. Geophys. Res.*, *93*(3), 2047–2052.
- Walker, J. A., M. J. Carr, L. C. Patino, C. M. Johnson, M. D. Feigenson, and R. L. Ward (1995), Abrupt change in magma generation processes across the Central American Arc in southeastern Guatemala: Flux-dominated melting near the base of the wedge to decompression melting near the top of the wedge, *Contrib. Mineral. Petrol.*, *120*(3–4), 378–390.

- Widiyantoro, S., B. L. N. Kennett, and R. D. van der Hilst (1999), Seismic tomography with P and S data reveals lateral variations in the rigidity of deep slabs, *Earth Planet. Sci. Lett.*, *173*(1–2), 91–100.
- Wiens, D. A., and G. P. Smith (2004), Seismological constraints on structure and flow patterns within the mantle wedge, in *Inside the Subduction Factory*, *Geophys. Monogr. Ser.*, vol. 138, edited by J. Eiler, pp. 57–81, AGU, Washington, D. C.
- Wiens, D. A., P. J. Shore, J. J. McGuire, E. Roth, M. G. Bevis, and K. Draunidalo (1995), The Southwest Pacific Seismic Experiment, *IRIS Newsl.*, *14*(1), 1–4.
- Wiens, D. A., K. Kelley, and T. Plank (2004), Mantle temperature variations in active back-arc basins inferred from seismology, petrology, and bathymetry, *Eos Trans. AGU*, *85*(47), Fall Meet. Suppl., Abstract T24B-02.
- Wiens, D. A., K. Kelley, and T. Plank (2006), Mantle temperature variations beneath back-arc spreading centers inferred from seismology, petrology, and bathymetry, *Earth Planet. Sci. Lett.*, in press.
- Willemann, R. J. (2001), Criteria for evaluating alternative hypocenters, analysis paper, Int. Seismol. Cent., Berkshire, UK.
- Wright, S. J., and J. N. Holt (1986), A new non-linear least squares algorithm for the seismic inversion problem, *Geophys. J. R. Astron. Soc.*, *87*(3), 1041–1056.
- Xu, Y., and D. A. Wiens (1997), Upper mantle structure of the southwest Pacific from regional waveform inversion, *J. Geophys. Res.*, *102*, 27,439–27,451.
- Yoshino, T., Y. Takei, D. A. Wark, and E. B. Watson (2005), Grain boundary wetness of texturally equilibrated rocks, with implications for seismic properties of the upper mantle, *J. Geophys. Res.*, *110*, B08205, doi:10.1029/2004JB003544.
- Zellmer, K. E., and B. Taylor (2001), A three-plate kinematic model for Lau Basin opening, *Geochem. Geophys. Geosyst.*, *2*(5), doi:10.1029/2000GC000106.
- Zhao, D., A. Hasegawa, and S. Horiuchi (1992), Tomographic imaging of P and S wave velocity structure beneath northeastern Japan, *J. Geophys. Res.*, *97*(13), 19,909–19,928.
- Zhao, D., Y. Xu, D. A. Wiens, L. Dorman, J. Hildebrand, and S. Webb (1997), Depth extent of the Lau back-arc spreading center and its relationship to the subduction process, *Science*, *278*, 254–257.